Suppression of phonon heat conduction in cross-section-modulated nanowires

D. L. Nika,[*] A. I. Cocemasov, and C. I. Isacova

E. Pokatilov Laboratory of Physics and Engineering of Nanomaterials, Department of Physics, Moldova State University,
Chisinau, MD-2009, Republic of Moldova

A. A. Balandin

Nano-Device Laboratory, Department of Electrical Engineering and Materials Science and Engineering Program,
University of California-Riverside, Riverside, California 92521, USA

V. M. Fomin and O. G. Schmidt

Institute for Integrative Nanosciences, IFW-Dresden, Dresden D-01069, Germany
(Received 8 February 2012; published 22 May 2012)

We have theoretically demonstrated that phonon heat flux can be significantly suppressed in Si and Si/SiO$_2$ nanowires with the periodically modulated cross-section area—referred to as the *cross-section-modulated* nanowires—in comparison with the generic uniform cross-section nanowires. The phonon energy spectra were obtained using the five-parameter Born–von Karman-type model and the face-centered-cubic cell model for description of the lattice dynamics. The thermal flux and thermal conductivity in Si and Si/SiO$_2$ cross-section-modulated nanowires were calculated from the Boltzmann transport equation within the relaxation time approximation. Redistribution of the phonon energy spectra in the cross-section-modulated nanowires leads to a strong decrease of the average phonon group velocities and a corresponding suppression of the phonon thermal flux in these nanowires as compared to the generic nanowires. This effect is explained by the exclusion of the phonon modes trapped in cross-section-modulated nanowires segments from the heat flow. As a result, a three- to sevenfold drop of the phonon heat flux in the 50- to 400-K temperature range is predicted for Si and Si/SiO$_2$ cross-section-modulated nanowires under consideration. The obtained results indicate that cross-section-modulated nanowires are promising candidates for thermoelectric applications.

I. INTRODUCTION

Heat transfer processes at nanoscale continue to attract significant attention.[1–7] Nanostructured materials with the high lattice thermal conductivity can be used as heat spreaders and interconnects[7–10] for enhanced heat removal from the nanoscale circuits. Materials with the low lattice thermal conductivity and high electrical conductivity are promising for thermoelectric applications since the measure of the efficiency of the thermoelectric energy conversion—figure of merit ZT—contains the electrical conductivity in the numerator and the lattice thermal conductivity in the denominator: $ZT = S^2 \sigma T / (\kappa_{ph} + \kappa_{el})$, where S is the Seebeck coefficient, σ is the electrical conductivity, T is the absolute temperature, and κ_{ph} and κ_{el} are the phonon, i.e., lattice and electron thermal conductivities, respectively. Acoustic phonons make the dominant contribution to the lattice heat conduction owing to their high group velocity and lower energy, resulting in the higher population factors.

Spatial confinement of acoustic phonons in nanostructures substantially changes their energy spectra and density of states in comparison with bulk materials, leading to a reduction of the phonon group velocities.[11–17] Modification of the phonon properties and enhancement of the phonon—boundary scattering stipulate lower values of the lattice thermal conductivity in nanostructures as compared with their bulk counterparts.[11–14,16] It has been demonstrated both experimentally and theoretically that the room-temperature (RT) lattice thermal conductivity in freestanding Si nanolayers, Si nanowires (NWs), planar Si/Ge superlattices, and Si/Ge

quantum dot superlattices is two orders of magnitude lower than the corresponding bulk value of Si.[6,18–23]

In spite of the fact that bulk Si is a poor thermoelectric with RT $ZT \sim 0.01$,[24] thin Si NWs and Si/Ge segmented NWs are considered promising for thermoelectric applications[6,25–28] owing to the much lower values of the RT lattice thermal conductivity $\kappa_{ph} < 1$ W m^{-1} K^{-1}. It has been demonstrated experimentally that the good electrical conductivity, as in doped bulk Si, and poor thermal conductivity of Si NWs[25] and rough Si NWs[26] provide relatively high values of $ZT \sim 0.3$ to 0.6 at RT. These experimental results stimulate theoretical search of one-dimensional Si-based nanostructured materials with the ultralow thermal conductivity. An up to 30-fold drop of the RT lattice thermal conductivity in comparison with Si NWs was reported for Si-based segmented NWs consisting of acoustically mismatched materials.[6] The reduction of the RT lattice thermal conductivity up to 75% was theoretically demonstrated in Si/Ge core-shell NWs with Ge thicknesses of several monoatomic layers.[29] The corresponding enhancement of ZT in these NWs was also predicted.[30]

In this paper, we show that a three- to sevenfold reduction of the lattice thermal conductivity can be achieved in the periodically cross-section-modulated Si and Si/SiO$_2$ NWs (MNWs) due to a strong redistribution of their phonon energy spectra in comparison with generic Si NWs. The phonon energy spectra in the MNWs and NWs under analysis were calculated using both the five-parameter Born–von Karman- (BvK-) type model[31–33] and the face-centered-cubic (fcc)[6] cell model of lattice dynamics. In the framework of our theoretical

approach, we demonstrate that the periodic cross-section modulation of Si NWs leads to more significant reduction of the lattice thermal conductivity than previously reported. The reduction is achieved in a wide temperature range from 50 to 400 K in the diffusive phonon transport regime.

Fabrication of the periodically cross-section-modulated NWs is still a major challenge. It is difficult to precisely control the shape and size of the nanowire segments. Nevertheless, various cross-section-modulated semiconductor NWs have already been fabricated using electrodeposition in the pores of anodic alumina membranes,[34] thermal evaporation,[35] metalorganic chemical vapor deposition,[36] and chemical vapor deposition.[37] The periodic diameter-modulated GeSi/Si pillar structures were prepared from the multilayer GeSi/Si islands using the selective etching of Si in KOH.[38] The theoretical models for the cross-section-modulated NWs have also been reported. The electron band structure in the size-modulated hydrogen-saturated Si NWs was calculated within the density-functional theory in Ref. [39]. Ballistic thermal conductance of Si and Si/Pb wires with modulation of the cross-sectional width from 0.1 to 0.5 μm was considered in Ref. [40]. Within the framework of the elasticity theory, thermal conductance was demonstrated to yield a minimum with a reduction by a factor 0.6 to 0.7 at $T \sim 0.1$ to 0.3 K.[40] NWs of GaAs modulated by several quantum dots reveal the enhanced thermoelectric properties at low temperatures in the ballistic transport regime due to modification of the electron transmission coefficients[41,42] and reduction of the low-temperature thermal conductance.[43]

The rest of the paper is organized as follows. In Sec. II we describe our theoretical approach for calculations of phonon energy spectra and thermal conductivity in generic and cross-section-modulated NWs. Results and discussions are presented in Sec. III. We give our conclusions in Sec. IV.

II. THEORETICAL MODEL

Numerous theoretical investigations of phonon properties of semiconductor nanostructures were carried out in the framework of a continuum approach. This approach is a powerful tool for the analysis of the long-wavelength phonon modes. It is completely adequate for the description of the electron-phonon interaction[44–46] or low-temperature thermal conductivity in nanostructures when only the low-frequency long-wavelength phonon modes are populated.[43,47] However, the continuum approach significantly overestimates thermal conductivity for temperatures $T > 100$ K in comparison with the fcc model of the lattice vibrations due to a steep slope of the dispersion curves for high-frequency phonon modes.[48] Different models of lattice dynamics and molecular dynamics simulations[4,5,48–53] allow for an accurate description of heat transfer and thermal conductivity in a good agreement with experiments.

We investigate the phonon and heat-conduction properties of the periodically cross-section-modulated rectangular Si NWs in the framework of the five-parameter BvK-type model of lattice dynamics and compare them with those of generic rectangular Si NWs. The schematics of the considered rectangular NW and MNW are shown in Fig. 1. The external surfaces of the nanostructures under consideration are assumed to be free.[6,13,15] The X and Y axes of the Cartesian coordinate
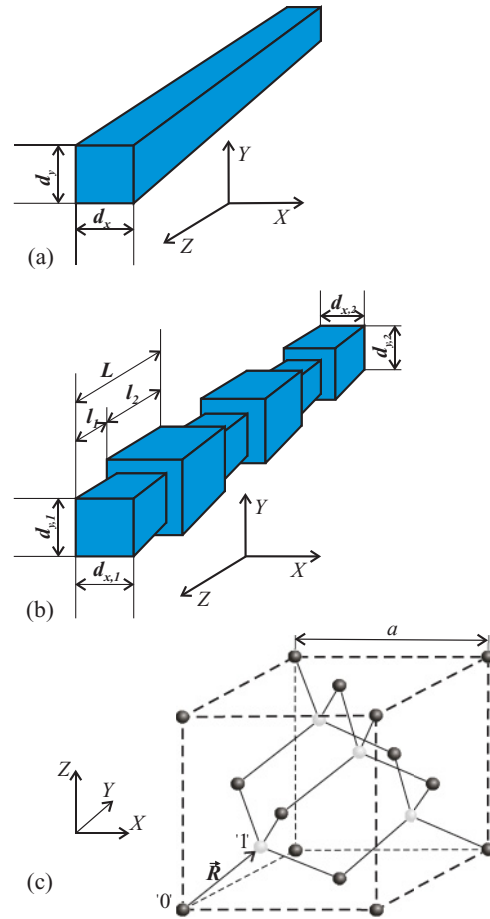

FIG. 1. (Color online) Schematic view of a rectangular nanowire (a), a rectangular cross-section-modulated nanowire (b), and a diamond-type crystal lattice (c).

system are located in the cross-sectional plane of the NWs (generic or modulated) and are parallel to its sides, while the Z axis is directed along the structure axis [see Figs. 1(a) and 1(b)]. We assume that NW and MNW are infinite along the Z axis. The origin of the coordinates is set at the center of the nanowire cross section. The translation period of MNW consists of two parts with dimensions $d_{x,1} \times d_{y,1} \times l_1$ and $d_{x,2} \times d_{y,2} \times l_2$, respectively. The length period of MNW is $L = l_1 + l_2$. The sides of NW are denoted as d_x and d_y.

The crystal lattice of Si consists of two fcc sublattices, which are shifted along the main diagonal of a unit cell by 1/4 of its length. For convenience, we identify the atoms of the first sublattice as the "dark" atoms, while we identify the atoms of the second sublattice as the "white" atoms [see Fig. 1(c)]. In nanostructures under consideration, the displacements of the atoms belonging to one period only are independent. The rest of the atomic displacements are equivalent to those in the selected period due to the translational symmetry along the Z axis. In the case of a generic NW, the translation period consists of two atomic layers of the "dark" atoms and two atomic layers of the "white" atoms (all layers are perpendicular to the Z axis). For MNW, the number of atomic layers in the period is determined by L. The displacements of equivalent atoms have the form

$$\vec{u}(x,y,z + n \cdot L; q_z) = \vec{w}(x,y,z; q_z)e^{iq_z(nL)}, \qquad (1)$$

where $\vec{w}(x,y,z;q_z) \equiv \vec{w}(\vec{r};q_z)$ is the displacement of the atom with coordinates x, y, and z, the period is labeled by an integer n, and q_z is the phonon wave number. The equations of motion for the displacement are

$$\omega^2 w_i(\vec{r}_k;q_z) = \sum_{j=x,y,z;\vec{r}_k'} D_{ij}(\vec{r}_k,\vec{r}_k')w_j(\vec{r}_k';q_z),$$
$$k = 1,\ldots,N, i = x,y,z, \qquad (2)$$

where

$$D_{ij}(\vec{r}_k,\vec{r}_k') = \Phi_{ij}(\vec{r}_k,\vec{r}_k')/\sqrt{m(\vec{r}_k)m(\vec{r}_k')}. \qquad (3)$$

In Eqs. (2) and (3), D_{ij} is the dynamic matrix coefficient, $m(\vec{r}_k)$ [$m(\vec{r}_k')$] is the mass of the atom at $\vec{r}_k$ [$\vec{r}_k'$], $\Phi_{ij}(\vec{r}_k,\vec{r}_k')$ is the matrix of force constants, and N is the number of atoms in the NW or MNW translational period. For the atom at $\vec{r}_k$, the summation in Eq. (2) is performed over all the nearest and second-nearest atoms at $\vec{r}_k'$. In the case of silicon, the atom at $\vec{r}_k$ has four nearest neighbors at $\vec{r}_{k,n}' = \vec{r}_k + \vec{h}_n^I$ ($n = 1,\ldots,4$) and 12 second-nearest neighbors at $\vec{r}_{k,n}' = \vec{r}_k + \vec{h}_n^{II}$ ($n = 1,\ldots,12$). The components of vectors $\vec{h}_n^I$ and $\vec{h}_n^{II}$ are presented in Table I. In our model, the interaction of an atom with its nearest and second-nearest neighbors is described by the following force constant matrices: $\Phi_{ij}^I = (16/a^2)(\alpha\delta_{ij} + \beta(1-\delta_{ij}))h_{n,i}^I h_{n,j}^I$ for the nearest atoms ($n = 1,\ldots,4$) and $\Phi_{ij}^{II} = (4/a^2)(\lambda\delta_{ij}(a^2/4 - h_{n,i}^{II}h_{n,i}^{II}) + \mu\delta_{ij}h_{n,i}^{II}h_{n,i}^{II} + \nu(1-\delta_{ij})h_{n,i}^{II}h_{n,j}^{II})$ for the second-nearest atoms ($n = 1,\ldots,12$), where a is the lattice constant, $\alpha, \beta, \mu, \lambda$, and ν are the force constants, δ_{ij} is the Kronecker delta and $i,j=x,y,z$. The force constant matrix $\Phi_{ij}(\vec{r}_k,\vec{r}_k' = \vec{r}_k)$ is obtained from the condition that the total force acting on the atom $\vec{r}_k$ at the equilibrium position is equal to 0, i.e., $\Phi_{ij}(\vec{r}_k,\vec{r}_k' = \vec{r}_k) + \sum_{\vec{r}_k'}\Phi_{ij}(\vec{r}_k,\vec{r}_k' \neq \vec{r}_k) = 0$.

By solving the equations of motion [Eq. (2)] at Γ and X Brillouin zone points of bulk Si, we expressed three constants α, μ, and λ of our model through β and the frequencies of the longitudinal optic (LO) and transverse optic (TO) phonons at Γ point and the longitudinal acoustic (LA) phonon at X point:

$$\alpha = m\omega_{LO}^2(\Gamma)/8,$$
$$\mu = m\left(2\omega_{LA}^2(X) - \omega_{LO}^2(\Gamma)\right)/32, \qquad (4)$$
$$\lambda = m\left(4\omega_{TO}^2(X) - 2\omega_{LA}^2(X) - \omega_{LO}^2(\Gamma)\right)/32 - \beta/2.$$

The constants β and ν were treated as fitting parameters and were obtained from the best fit to experimental dispersion curves for bulk Si.[54] The numerical values of the force constants for Si are indicated in the last column of Table I.

For calculation of the phonon heat flux per unit temperature gradient in the NWs and the MNWs, we use the following expression, which was derived from the Boltzmann transport equation within the relaxation time approximation,[4,16,48,49] taking into account one-dimensional density of phonon states:[6]

$$\Theta = \frac{1}{2\pi k_B T^2} \sum_{s=1,\ldots,3N} \int_0^{q_{z,\max}} (\hbar\omega_s(q_z)\upsilon_{z,s}(q_z))^2$$
$$\times \tau_{\text{tot},s}(q_z)\frac{\exp\left(\frac{\hbar\omega_s(q_z)}{k_B T}\right)}{\left(\exp\left(\frac{\hbar\omega_s(q_z)}{k_B T}\right) - 1\right)^2}dq_z. \qquad (5)$$

Here $\tau_{\text{tot},s}$ is the total phonon relaxation time, s is the number of a phonon branch, k_B is the Boltzmann constant, $\hbar$ is the Planck constant, T is the absolute temperature, $q_{z,\max} = \pi/L$ for MNWs and $q_{z,\max} = \pi/a$ for NWs (in the case of NWs, $L = a$). In our calculations, we take into account all basic mechanisms of phonon scattering: three-phonon umklapp scattering, boundary and impurity scatterings.[6,11,16,48–53] According to the Matthiessen's rule, the total phonon relaxation time is given by: $1/\tau_{\text{tot},s}(q_z) = 1/\tau_{U,s}(q_z) + 1/\tau_{\text{imp},s}(q_z) + 1/\tau_{B,s}(q_z)$. Here, (i) $\tau_{U,s}$ is the relaxation time for the umklapp scattering: $\frac{1}{\tau_{U,s}(q_z)} = B(\omega_s(q_z))^2 T \exp(-C/T)$;[16] (ii) $\tau_{\text{imp},s}$ is the relaxation time for the impurity scattering $\frac{1}{\tau_{\text{imp},s}(q_z)} = A(\omega_s(q_z))$;[4,6,16] and (iii) $\tau_{B,s}$ is the relaxation time for the boundary scattering:

$$\frac{1}{\tau_{B,s}(q_z)} = \frac{1-p}{1+p}\frac{|\upsilon_{z,s}(q_z)|}{2}\left(\frac{1}{d_x} + \frac{1}{d_y}\right), \qquad (6)$$

TABLE I. Components of the nearest and second-nearest atoms $\vec{r}_{k,n}' = \vec{r}_k + \vec{h}_n^{I(II)}$ in the diamond-type unit cell and a set of the force constants used for Si.

Components of vectors $\vec{h}_n^I$ for the selected "white" atom $\vec{r}_k$	Components of vectors $\vec{h}_n^I$ for the selected "dark" atom $\vec{r}_k$	Components of vectors $\vec{h}_n^{II}$ for the selected "white" (or "dark") atom $\vec{r}_k$	Set of five force constants of silicon used for calculation (N/m)
$a/4(1,1,1)$	$a/4(-1,-1,-1)$	$a/2(1,1,0)$	$\alpha = 54.85$
$a/4(1,-1,-1)$	$a/4(-1,1,1)$	$a/2(-1,-1,0)$	$\beta = 35.0$
$a/4(-1,1-1)$	$a/4(1,-1,1)$	$a/2(1,0,1)$	$\mu = 3.8$
$a/4(-1,-1,1)$	$a/4(1,1,-1)$	$a/2(-1,0,-1)$	$\nu = 2.5$
		$a/2(0,1,1)$	$\lambda = -4.42$
		$a/2(0,-1,-1)$	
		$a/2(-1,1,0)$	
		$a/2(1,-1,0)$	
		$a/2(-1,0,1)$	
		$a/2(1,0,-1)$	
		$a/2(0,-1,1)$	
		$a/2(0,1,-1)$	

in the case of a NW, and

$$\frac{1}{\tau_{B,s}(q_z)} = \frac{1-p}{1+p} \frac{|\upsilon_{z,s}(q_z)|}{2} \left(\left(\frac{1}{d_{x,1}} + \frac{1}{d_{y,1}} \right) \int_{-d_{x,1}/2}^{d_{x,1}/2} \int_{-d_{y,1}/2}^{d_{y,1}/2} \int_0^{l_1} |\vec{w}_s(x,y,z;q_z)|^2 \, dx\,dy\,dz \right.$$
$$\left. + \left(\frac{1}{d_{x,2}} + \frac{1}{d_{y,2}} \right) \int_{-d_{x,2}/2}^{d_{x,2}/2} \int_{-d_{y,2}/2}^{d_{y,2}/2} \int_{l_1+a/4}^{l_1+l_2} |\vec{w}_s(x,y,z;q_z)|^2 \, dx\,dy\,dz \right), \tag{7}$$

in the case of a MNW. In Eqs. (6) and (7), $\upsilon_{z,s}(q_z) = d\omega_s(q_z)/dq_z$ is the phonon group velocity along the nanowire axis, and p is the specularity parameter of the boundary scattering. Equations (6) and (7) provide an extension of the standard formula for the rough edge scattering[55] to the case of a rectangular NW or MNW. In Eq. (7) we take into account that a part of the phonon wave corresponding to the mode (s,q_z), concentrated in the MNW segment $d_{x,1} \times d_{y,1} \times l_1$, scatters on the boundaries of this segment, while the rest of this wave scatters on the boundaries of the segment $d_{x,2} \times d_{y,2} \times l_2$. Parameters A, B, and C were fitted from a comparison of the thermal conductivity calculated for bulk silicon with experimental data.[56] In the present work, we obtained the following values for these parameters: $A = 1.32 \times 10^{-9}$ s^3, $B = 1.88 \times 10^{-19}$ s/K, and $C = 137.39$ K.

III. RESULTS AND DISCUSSION

To calculate the energy spectra of phonons in Si NWs and MNWs, we numerically solve the set of Eqs. (2) by taking into account the periodic boundary conditions [see Eq. (1)] along the Z axis and free-surface boundary conditions in the XY plane (i.e., all force constants outside the nanostructure are set to zero). We perform calculations for all q_z values in the interval $(0, \pi/L)$ for MNWs and $(0, \pi/a)$ for NWs. The notations and dimensions in the monoatomic layers (ML; 1 ML $= a/4$) for Si NWs and MNWs analyzed in the present work are represented in Table II.

The phonon energy spectra of Si NW 1 and Si MNW 1 are shown in Figs. 2(a) and 2(b), correspondingly. In the figure, we show 20 lowest branches $\hbar\omega_s(q_z)$ ($s = 1,2,\ldots,20$) in both structures as well as several higher branches with $s = 20,25,30,35,\ldots, 285,290,294$ for the NW and with $s = 35,50,65,80,\ldots,1515,1530$ for the MNW. The nanowire cross section is chosen the same as the cross section of narrow segments of the MNW (see Table II). The volume of a translational period in the MNW is larger than that in the NW; therefore, the number of quantized phonon branches in the MNW is substantially larger as compared to the NW. In the MNW, there are 1530 branches, while only 294 branches exist in the NW (see Fig. 2). As follows from Fig. 2, a great number of phonon modes in the MNW with energy $\hbar\omega > 5$ meV are dispersionless and possess group velocities close to zero due to the trapping into the MNW segments. The trapping effect is illustrated in Fig. 3: the average squared displacements of

TABLE II. Notations and dimensions for Si NWs and cross-section-modulated NWs under consideration.

Nanostructure	Dimensions	Notation in the present work
Si NW	14 × 14 ML	NW 1
Si MNW	14 × 14 × 6 ML/22 × 22 × 6 ML	MNW 1
Si MNW	14 × 14 × 8 ML/18 × 18 × 8 ML	MNW 2
Si MNW	14 × 14 × 8 ML/22 × 22 × 8 ML	MNW 3
Si MNW	14 × 14 × 8 ML/26 × 26 × 8 ML	MNW 4
Si MNW	14 × 14 × 8 ML/30 × 30 × 8 ML	MNW 5
Si MNW	14 × 14 × 8 ML/34 × 34 × 8 ML	MNW 6
Si MNW	14 × 14 ML × N_z/22 × 22 ML × N_z	MNW 7
Si MNW	14 × 14 × 4 ML/22 × 22 × 4 ML	MNW 8
Si MNW	14 × 14 × 4 ML/22 × 22 × 12 ML	MNW 9
Si/SiO$_2$ MNW	Si(14 × 14 × 12 ML)/SiO$_2$(18 × 18 × 12 ML)	MNW 10
	Si(14 × 14 × 12 ML)/SiO$_2$(22 × 22 × 12 ML)	
Si/SiO$_2$ MNW	Si(30 × 30 × 12 ML)/SiO$_2$(38 × 38 × 12 ML)	MNW 11
	Si(30 × 30 × 12 ML)/SiO$_2$(46 × 46 × 12 ML)	
Si/SiO$_2$ MNW	Si(30 × 30 × 12 ML)/SiO$_2$(34 × 34 × 12 ML)	MNW 12
	Si(30 × 30 × 12 ML)/SiO$_2$(38 × 38 × 12 ML)	
Si/SiO$_2$ MNW	Si(14 × 14 × 12 ML)	MNW 13
	Si(14 × 14 × 12 ML)/SiO$_2$(18 × 18 × 12 ML)	
Si/SiO$_2$ MNW	Si(14 × 14 × 12 ML)	MNW 14
	Si(14 × 14 × 12 ML)/SiO$_2$(26 × 26 × 12 ML)	
Si/SiO$_2$ MNW	Si(30 × 30 × 12 ML)	MNW 15
	Si(30 × 30 × 12 ML)/SiO$_2$(38 × 38 × 12 ML)	

atoms [see Fig. 3(a)]

$$|U(z;s,q_z)|^2 = \begin{cases} \int_{-d_{x,1}/2}^{d_{x,1}/2} \int_{-d_{y,1}/2}^{d_{y,1}/2} |\vec{w}_s(x,y,z;q_z)|^2 \, dxdy, & \text{if } 0 \leqslant z \leqslant l_1 \\ \int_{-d_{x,2}/2}^{d_{x,2}/2} \int_{-d_{y,2}/2}^{d_{y,2}/2} |\vec{w}_s(x,y,z;q_z)|^2 \, dxdy, & \text{if } l_1 < z \leqslant l_2 \end{cases} \quad (8)$$

in the mode [$s = 8$, $q_z = 0.4q_{z,\max}$; red (medium gray)] line are relatively large in the wide segments of the MNW and almost vanishing in the narrow segments. Therefore, this mode is trapped into the wide segments of the MNW. For comparison, we also show the average squared displacements of atoms in a propagating phonon mode [$s = 992$, $q_z = 0.2q_{z,\max}$; blue (light gray)] line , which are equally large in both the wide and narrow MNW segments. For illustration of the phonon mode distribution in the cross section of MNWs in Fig. 3(b), we show the integral squared displacements of atoms in 14×14 ML cross-section channel as a function of the phonon energy:

$$U_{\text{core}}^2 = \int_{-d_{x,1}/2}^{d_{x,1}/2} \int_{-d_{y,1}/2}^{d_{y,1}/2} \int_0^{l_1+l_2} |\vec{w}_s(x,y,z;q_z(\omega))|^2 \, dxdydz. \quad (9)$$
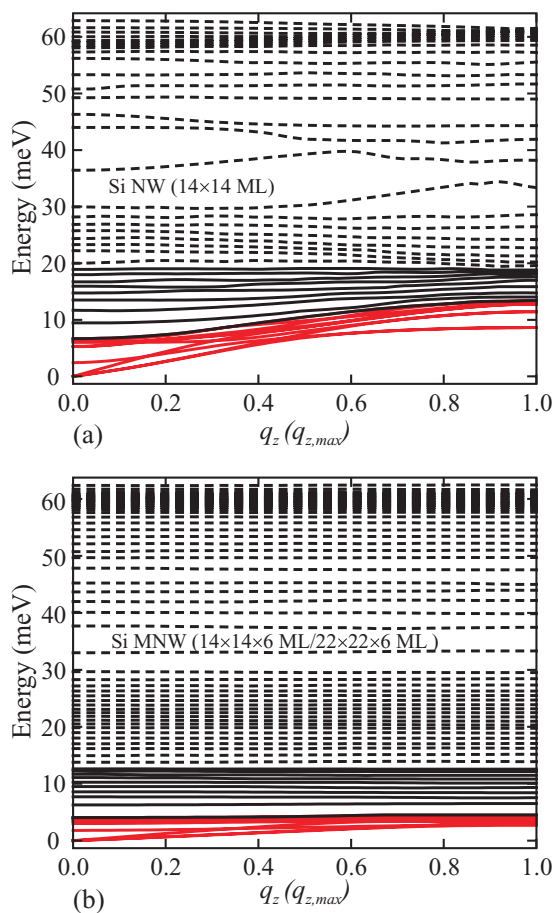
The results are presented for NW 1 (dashed black line) and MNW 2 (red dots), MNW 4 (green stars), and MNW 6 (blue triangles). In Si NW $U_{\text{core}}^2 = 1$ for all energies due to the orthonormalization of the phonon displacement vectors [see dashed black line in Fig. 3(b)]. Increase of the cross section of the wide segments leads to the decrease of U_{core}^2 for all phonon energies and, correspondingly, the rise of $(1 - U_{\text{core}}^2)$. The latter is indicative of the phonon mode localization in the wide
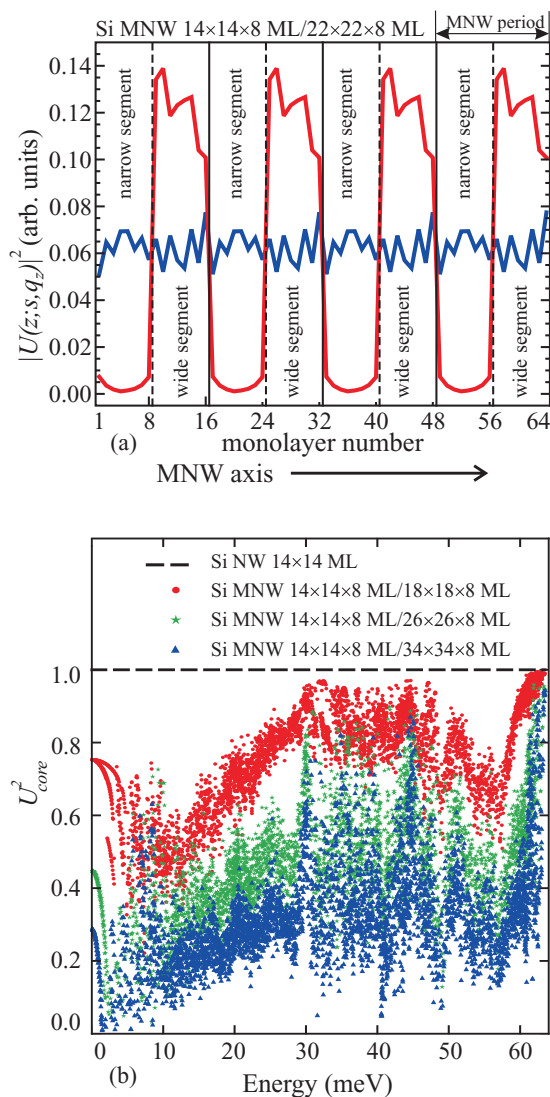

FIG. 2. (Color online) Phonon energies as a function of the phonon wave vector q (a) in Si NW with the lateral cross section 14×14 ML (the phonon branches with $s = 1$ to $20, 25, 30, 35 \ldots 290,$ 294 are shown) and (b) in Si MNW with dimensions $14 \times 14 \times 6$ ML$/22 \times 22 \times 6$ ML. The phonon branches with $s = 1$ to $20, 35,$ $50, 65, \ldots, 1515, 1530$ are depicted.

FIG. 3. (Color online) (a) Average squared displacements $|U(z;s,q_z)|^2$ of the trapped [$s = 8$, $q_z = 0.4q_{z,\max}$; red (medium gray) line] and propagating [$s = 992$, $q_z = 0.2q_{z,\max}$; blue (light gray) line] phonon modes in Si MNW with dimensions $14 \times 14 \times 8$ ML$/22 \times 22 \times 8$ ML. (b) Localization of phonon modes in 14×14 ML MNW core shown for MNWs 2, 4, and 6.
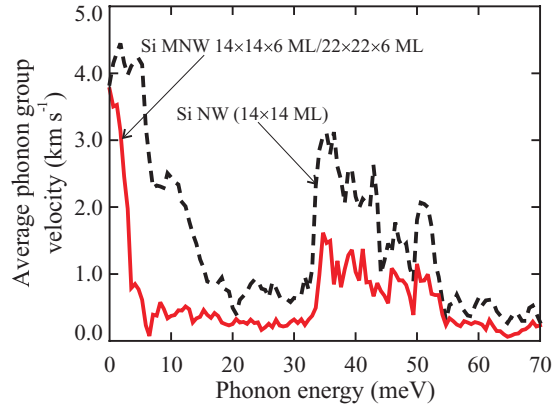
FIG. 4. (Color online) Average phonon group velocity as a function of the phonon energy in Si NW with the lateral cross section 14×14 ML and Si MNW with dimensions $14 \times 14 \times 6$ ML/$22 \times 22 \times 6$ ML.

FIG. 5. (Color online) Temperature dependence of the lattice thermal conductivity in Si NW with the cross section 14×14 ML and Si MNWs 2–5.

segments. Thus, the trapping effect enhances with increasing cross section of the wide segments.

The effect of the phonon deceleration in cross-section-modulated NWs is illustrated in Fig. 4, where we show the average phonon group velocity $\langle v \rangle (\omega) = g(\omega) / \sum_{s(\omega)} (d\omega_s / dq_z)^{-1}$ as a function of the phonon energy for Si NW 1 (dashed line) and Si MNW 1 (solid line). Here summation is performed over all phonon modes $s(\omega)$ with the frequency ω; $g(\omega)$ is the number of the phonon modes. The average phonon group velocity in MNW is smaller than that in the NW for all phonon energies. As a result, the phonon modes in MNW carry less heat than those in the NW. The drop in the phonon group velocities in MNWs in comparison with NWs is explained by the trapping effect: the trapped phonon modes represent standing waves existing only in the wide segments of MNWs. These modes do not penetrate into narrow MNW segments [see the red (medium gray) line in Fig. 3(a)]. Therefore, these phonons possess group velocities close to zero. For example, group velocities of the phonon modes shown in Fig. 3(a) are $v_{z,s=992}(q_z = 0.2 \cdot q_{z,\max}) \sim 1.5$ km/s and $v_{z,s=8}(q_z = 0.4 \cdot q_{z,\max}) \sim 0.01$ km/s for the propagating and trapped modes, respectively. A similar strong reduction of the phonon group velocity has been recently demonstrated in the segmented NWs, consisting from the acoustically mismatched materials.[6] The effect was also explicated by the phonon modes trapping in the NW segments.

In Fig. 5, the lattice thermal conductivity $\kappa_{\mathrm{ph}}^{\mathrm{NW}} = \Theta / (d_x d_y)$ and $\kappa_{\mathrm{ph}}^{\mathrm{MNW}} = \Theta (l_1 + l_2) / (d_{x,1} d_{y,1} l_1 + d_{x,2} d_{y,2} l_2)$ are plotted as a function of temperature for Si NW 1, as well as for Si MNWs 2–5. The results are presented for a reasonable specularity parameter $p = 0.85$, which was found in Ref. 53 from a comparison between theoretical and experimental data for a Si film of 20-nm thickness. A significant redistribution of the phonon energy spectra and a reduction of the average group velocities in MNWs strongly decrease their lattice thermal conductivity in comparison with the NW. At RT, the ratio between the thermal conductivities in NW and MNWs ranges from a factor of 5 to 13, depending on $S_2 = d_{x,2} \times d_{y,2}$. However, this result does not mean that the ratio of the thermal fluxes in NW and MNWs should be the same since the average
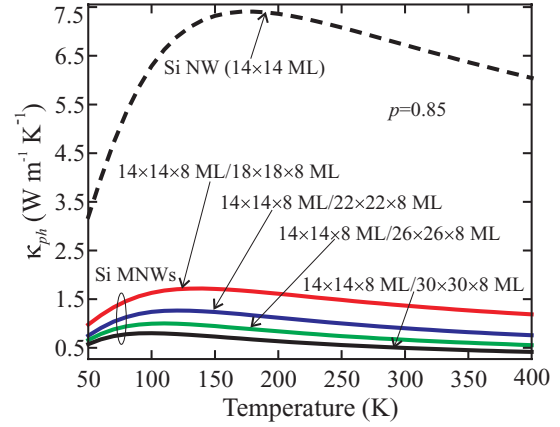
cross section of MNWs is larger than that in NW. To compare the abilities of MNWs and NWs to conduct heat, we calculated the thermal flux per unit temperature gradient Θ, referred to as the thermal flux hereafter in the paper, using Eq. (5) for all structures under analysis.

In Fig. 6(a) we show the thermal flux for Si NW 1 (upper dashed line) and Si MNWs 2, 4, and 6 for $p = 0.85$ as a function of temperature. The maxima on the thermal flux curves are determined by the interplay between the three-phonon umklapp and the phonon boundary scattering. At low temperatures, the boundary scattering dominates; the thermal flux increases with temperature due to the population of high-energy phonon modes and approaches the maximum value when $\tau_U \sim \tau_B$. A subsequent rise of temperature leads to an enhancement of the umklapp scattering and diminution of the thermal flux. An increase of the cross section of the MNW wide segments attenuates the phonon boundary scattering, and the maximum of the thermal flux curves shifts to lower temperatures: from $T = 190$ K for Si NW 1 to $T = 100$ K for Si MNW 6. Therefore, at low temperatures ($T < 120$ K), the thermal flux reduction is stronger in MNWs with the smaller cross sections. Numerous high-energy phonon modes in MNWs are trapped in the wide segments and possess a low group velocity. The population of these modes with increasing temperature almost does not increase the thermal flux. Thus, at medium and high temperatures, the umklapp-limited thermal flux in MNWs reduces stronger than that in the generic NW. The ratio of the thermal fluxes in NW and MNW $\eta = \Theta(\mathrm{Si\ NW}) / \Theta(\mathrm{Si\ MNW})$ increases with temperature and reaches the values of 3.5 to 4, depending on the MNW cross section [see Fig. 6(b)]. For these temperatures, the increase of the MNW cross section makes the reduction of the thermal flux stronger due to the corresponding rise of the number of the trapped high-energy phonon modes, which do not carry heat in MNWs. This is distinct from the case of NWs. The strong modification of the phonon energy spectra and phonon group velocities in MNWs in comparison with NWs also increases the umklapp phonon scattering in MNWs as compared with NWs. The latter is an additional reason for the thermal flux reduction in MNWs.
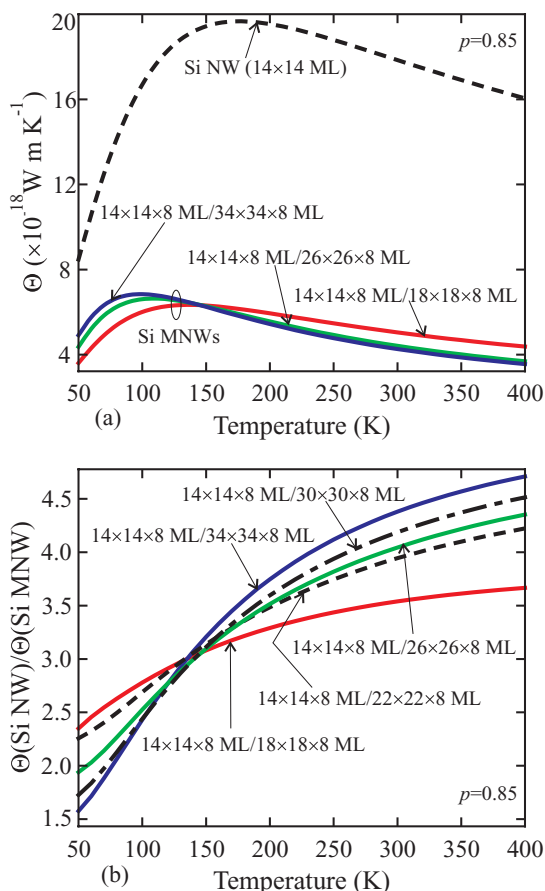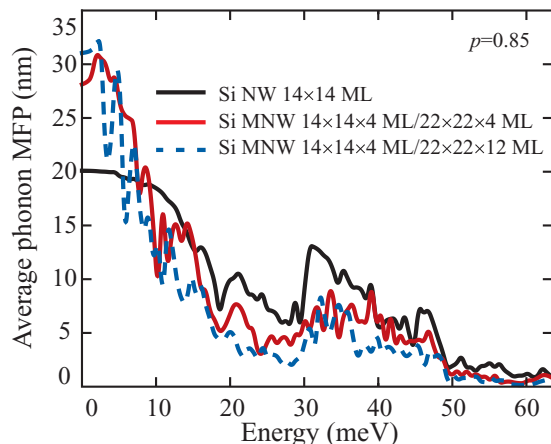
FIG. 7. (Color online) Dependence of the average phonon MFP on the phonon energy in Si NW 1 (solid black line) and Si MNW 8 [solid red (medium gray) line], and MNW 9 (dashed blue line).

when the umklapp scattering is weaker than the boundary scattering $\langle\Lambda\rangle^{MNW} > \langle\Lambda\rangle^{NW}$, while for $\hbar\omega > 5$ meV $\langle\Lambda\rangle^{MNW} \ll \langle\Lambda\rangle^{NW}$. Nevertheless, the integrand in Eq. (5) averaged over all phonon branches is smaller in MNWs for all energies due to the multiplication of $\Lambda_s(q_z)$ by $\upsilon_{z,s}(q_z)$ [see Eq. (5)]. The augmentation of l_2 decreases $\langle\Lambda\rangle^{MNW}$ for almost all energies. The energy-averaged phonon MFP calculated from Fig. 7 constitutes $\sim$9.25 nm for the Si NW, $\sim$8.4 nm for the MNW 8, and $\sim$6.9 nm for the MNW 9. The increase in the average MNW cross section at fixed l_1 and l_2 attenuates boundary scattering and increases the thermal flux.

In Fig. 8 we show the dependence of the ratio η of the thermal fluxes in Si NW 1 and Si MNW 3 on temperature for different values of the specularity parameter $p = 0.0, 0,3,$ 0.6, and 0.9. For the interpretation of the data in Fig. 8, we have separately calculated the thermal flux Θ_B carried out by the long-wavelength phonon modes (s,q_z), which are mainly scattered at the boundaries and described by the inequality $\tau_U(s,q_z) \geqslant \tau_B(s,q_z)$, and the thermal flux Θ_U carried out by the rest of the phonons, with the total thermal flux being $\Theta = \Theta_B + \Theta_U$. Our results show that for all values of p

FIG. 6. (Color online) (a) Temperature dependence of the thermal flux for Si NW (dashed line) and Si MNWs with dimensions $14 \times 14 \times 8$ ML/$18 \times 18 \times 8$ ML, $14 \times 14 \times 8$ ML/$26 \times 26 \times 8$ ML and $14 \times 14 \times 8$ ML/$34 \times 34 \times 8$ ML. (b) Temperature dependence of the ratio between thermal fluxes in Si NW and Si MNWs. The dimensions in the graph are indicated in monoatomic layers (ML).

An important quantity, which determines the thermal conductivity and thermal flux, is the mode-dependent phonon mean-free path (MFP) $\Lambda_s(q_z)$. In our model $\Lambda_s(q_z)$ is given by

$$1/\Lambda_s(q_z) = \sum_{r=B,U,\text{imp}} 1/\Lambda_{r,s}(q_z), \qquad (10)$$

where $\Lambda_{r,s}(q_z) = \tau_{r,s}(q_z) \cdot \upsilon_{z,s}(q_z)$ and $r = B$, U, or imp. Since the impurity scattering for the chosen parameter A is by two orders of magnitude smaller than the umklapp and phonon boundary scatterings, we discuss here only the interplay between $\Lambda_{B,s}(q_z)$ and $\Lambda_{U,s}(q_z)$. The dependence of the average phonon MFP $\langle\Lambda\rangle(\omega) = g(\omega)/\sum_{s(\omega)}(1/\Lambda_s)$ on the phonon energy is presented in Fig. 7 for the NW 1 (solid black line) and MNW 8 [solid red (medium gray) line] and MNW 9 (dashed blue line). The umklapp-limited phonon MFPs $\Lambda_{U,s}(q_z)$ in MNWs are significantly smaller than those in NWs due to both reduction of the group velocity and enhancement of the phonon scattering. The boundary-limited MFPs $\Lambda_{B,s}(q_z)$ are larger in MNWs due to the larger average cross section of MNW in comparison with that in NW [see Eqs. (6) and (7)]. As a result, at small energies
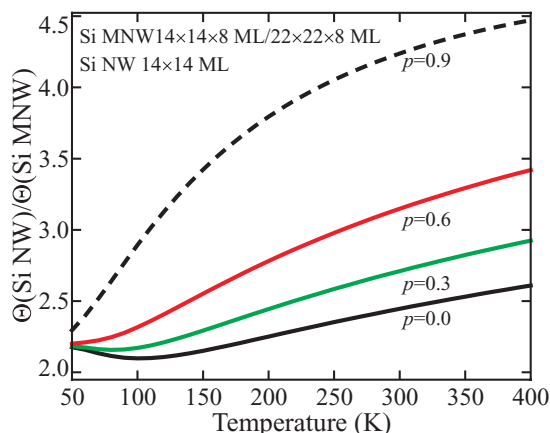

FIG. 8. (Color online) Temperature dependence of the ratio of thermal fluxes in Si NW and Si MNWs. The results are shown for different values of the specularity parameter $p = 0.0$, 0.3, 0.6, and 0.9.

under consideration, the RT flux Θ_B is by a factor of $\sim$5 lower in MNW than that in NW due to the phonon trapping. An increase of p decreases Θ_B and strongly enhances Θ_U in NW due to attenuation of the boundary scattering of the high-energy phonon modes. These modes in MNW do not participate in the heat transfer because of their localization in the wide segments. For this reason, the ratio between thermal fluxes in the NW and the MNW appreciably depends on p: for $p = 0.0$ $\Theta_U(\text{NW})/\Theta_U(\text{MNW}) \sim 1$, while for $p = 0.9$ $\Theta_U(\text{NW})/\Theta_U(\text{MNW}) \sim 3$. As a result, the flux ratio increases with increasing p in a wide range of temperatures from 100 to 400 K. The RT thermal conductivity of the rough Si NWs[26] is already by a factor of 100 lower than the corresponding bulk value. Our results suggest that the cross-section modulation of the rough NWs allows for an additional decrease of the thermal conductivity by a factor of 2 to 2.5 with a subsequent increase of ZT.

The dependence of the ratio η of the thermal fluxes in Si NW 1 and Si MNW 7 on N_z for the temperatures $T = 100$ K, $T = 200$ K, $T = 300$ K, and $T = 400$ K and $p = 0.85$ is presented in Fig. 9. The calculated points for $N_z = 2, 4, 6, \ldots, 18$ are joined by the smooth curves as guides for an eye. The overall trend of these curves is determined by the interplay of two effects: (i) the phonon modes trapping, which suppresses the heat flux and (ii) augmentation of the MNW average cross section, which enhances the heat flux due to the emergence of additional phonon modes for heat propagation and attenuation of the phonon boundary scattering. In Si MNW with the ultranarrow segments $N_z = 2$ ML, the trapping of phonon modes is weak, and the thermal flux is larger than that in Si NW ($\eta < 1$) due to the weakening of the phonon boundary scattering in MNW in comparison with NWs. The rise of N_z enhances the trapping, and for all temperatures under consideration, the flux ratios rapidly increase with N_z rising up to the values 8 to 12 ML and reach their maximum values at around $N_z = 16$ to 18 ML. We expect that a subsequent rise of N_z should decrease η due to augmentation of the MNW average cross section. Nevertheless, additional investigation of this limiting case is required. The latter is beyond the scope of the present work and will be addressed elsewhere.
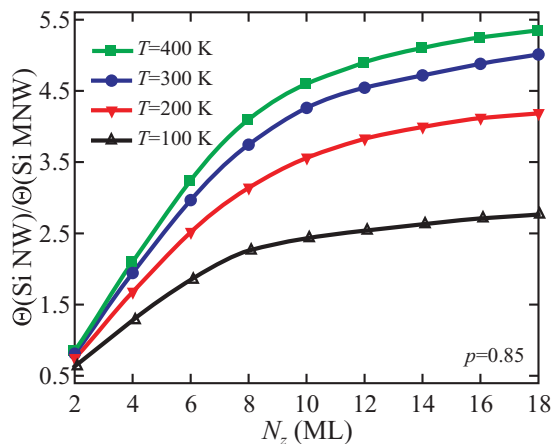
The acoustically mismatched cladding layers (coatings) strongly influence phonon properties and the lattice thermal conductivity of planar multilayer nanostructures and coated NWs.[1,6,13,15,29,53,57] To investigate the effect of the cross-section-modulated coatings, we consider Si NWs (cores) coated with the model SiO_2 cross-section-modulated shells (see MNWs 10–15 from Table II). The calculation of the phonon energy spectra in Si/SiO_2 MNWs are performed in the framework of the fcc model of lattice dynamics.[6,53,57] The fcc model is based on the three force constants, which are expressed through the independent elastic constants of the material. This model is one of the simplified models of lattice dynamics, which is suitable for the description of acoustic properties of heterostructures consisting of layers with different acoustic properties. A detailed description of this model has been recently presented by some of the present authors in Ref. 6. We assume also that the model SiO_2 material possesses the same crystal structure as Si but has elastic constants and density of real SiO_2: $c_{11} = 76.6$ GPa, $c_{12} = 14.8$ GPa, $c_{44} = 30.9$ GPa, and $\rho = 2.2$ g cm^{-3}.[6]

In Fig. 10 we show the ratio η of the thermal flux in Si NW 1 and Si/SiO_2 MNWs 10–15 as a function of temperature. The heat flux in Si/SiO_2 MNWs drops by a factor of 3 to 7, depending on the MNW core and shell dimensions. The reason for the thermal flux reduction is the same as in the case of Si MNWs: decrease of the average phonon group velocity and trapping of phonon modes into the MNW segments. In Si NWs, partially coated with SiO_2 (MNWs 13–15), the heat propagates only through Si core, while in Si NWs fully coated with SiO_2 (MNWs 10–12), it propagates also through SiO_2 shell. As a result, reduction of the heat flux is stronger in the MNWs 13–15 in comparison with that in the MNWs 10–12. In general, more complicated lattice dynamics models than the fcc model are needed for an accurate quantitative description of Si/SiO_2 MNWs. Therefore, our results presented here provide a qualitative description of their thermal properties. Nevertheless, we have checked that the fcc model, only by a few ($\sim$2 to 10) percent, overestimates the heat flux in Si NWs and MNWs in comparison with the five-parameter BvK model due to the difference in phonon dispersion curves.
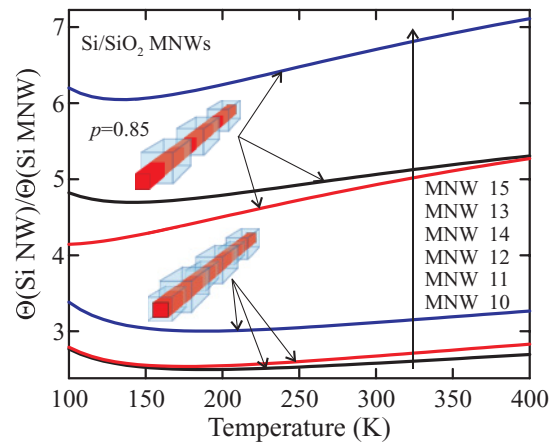
FIG. 9. (Color online) Ratio of thermal fluxes in Si NW and Si MNWs as a function of N_z. The results are shown for different temperatures $T = 100, 200, 300,$ and 400 K.

FIG. 10. (Color online) Ratio of thermal fluxes in Si NW and Si/SiO_2 MNWs as a function of temperature. The results are shown for different Si/SiO_2 MNWs 10 to 15 (see Table II for the notations).

IV. CONCLUSIONS

We theoretically investigated the phonon and thermal properties of Si and Si/SiO$_2$ cross-section-modulated NWs in the framework of the five-parameter Born-von Karman-type and the fcc models of lattice dynamics. A large number of phonon modes in MNWs are trapped into MNWs segments. As a result, the three- to sevenfold drop of the phonon heat flux in a wide temperature range from 50 to 400 K is reached for Si and Si/SiO$_2$ cross-section-modulated NWs in comparison with the generic Si NWs. We predict a similar effect for the cross-section-modulated NWs made of other materials. The obtained results indicate that the cross-section-modulated NWs are excellent candidates for applications as thermoelectric materials or thermal insulators.

*Corresponding author: dlnika@yahoo.com

[1] M. Hu, X. Zhang, K. P. Giapis, and D. Poulikakos, Phys. Rev. B **84**, 085442 (2011).

[2] J. Carrete, L. J. Gallego, L. M. Varela, and N. Mingo, Phys. Rev. B **84**, 075403 (2011).

[3] K. Esfarjani, G. Chen, and H. T. Stokes, Phys. Rev. B **84**, 085204 (2011).

[4] D. L. Nika, E. P. Pokatilov, A. S. Askerov, and A. A. Balandin, Phys. Rev. B **79**, 155413 (2009).

[5] A. Kundu, N. Mingo, D. A. Broido, and D. A. Stewart, Phys. Rev. B **84**, 125426 (2011).

[6] D. L. Nika, E. P. Pokatilov, A. A. Balandin, V. M. Fomin, A. Rastelli, and O. G. Schmidt, Phys. Rev. B **84**, 165415 (2011).

[7] S. Gosh, W. Bao, D. L. Nika, S. Subrina, E. P. Pokatilov, C. N. Lau, and A. A. Balandin, Nat. Mater. **9**, 555 (2010).

[8] Q. Shao, G. Liu, D. Teweldebrhan, and A. A. Balandin, Appl. Phys. Lett. **92**, 202108 (2008).

[9] R.-H. Horng, R.-C. Lin, H.-L. Hu, K.-C. Peng, and C.-P. Hsu, Electrochem Solid-State Lett. **14**, H453 (2011).

[10] G. Ko and J. Kim, Electrochem Solid-State Lett. **12**, H29 (2009).

[11] A. Balandin and K. L. Wang, Phys. Rev. B **58**, 1544 (1998).

[12] C. Colvard, T. A. Gant, M. V. Klein, R. Merlin, R. Fischer, H. Morkoc, and A. C. Gossard, Phys. Rev. B **31**, 2080 (1985).

[13] A. A. Balandin, E. P. Pokatilov, and D. L. Nika, J. Nanoelect. Optoelect. **2**, 140 (2007).

[14] R. Venkatasubramanian, Phys. Rev. B **61**, 3091 (2000).

[15] E. P. Pokatilov, D. L. Nika, and A. A. Balandin, Phys. Rev. B **72**, 113311 (2005).

[16] N. Mingo, Phys. Rev. B **68**, 113308 (2003).

[17] E. P. Pokatilov, D. L. Nika, and A. A. Balandin, Superlatt. Microstruct. **38**, 168 (2005).

[18] A. Khitun, A. Balandin, and K. L. Wang, Superlatt. Microstruct. **26**, 181 (1999).

[19] D. Li, Y. Wu, P. Kim, L. Shi, P. Yang, and A. Majumdar, Appl. Phys. Lett. **83**, 3186 (2003).

[20] W. Liu and M. Asheghi, J. Heat Transfer **128**, 75 (2006).

[21] G. Pernot, M. Stoffel, I. Savic, F. Pezzoli, P. Chen, G. Savelli, A. Jacquot, J. Schumann, U. Denker, I. Monch, C. Deneke, O. G. Schmidt, J. M. Rampnoux, S. Wang, M. Plissonnier, A. Rastelli, S. Dilhaire, and N. Mingo, Nat. Mater. **9**, 491 (2010).

[22] S.-M. Lee, D.G. Cahill, and R. Venkatasubramanian, Appl. Phys. Lett. **70**, 2957 (1997).

[23] B. Yang, W. L. Liu, K. L. Wang, and G. Chen, Appl. Phys. Lett. **81**, 3588 (2002).

[24] L. Weber and E. Gmelin, Appl. Phys. A **53**, 136 (1991).

[25] A. I. Boukai, Y. Bunimovich, J. Tahir-Kheli, J.-K. Yu, W. A. Goddard III, and J. R. Heath, Nature **451**, 168 (2007).

[26] A. I. Hochbaum, R. Chen, R. D. Delgado, W. Liang, E. C. Garnett, M. Najarian, A. Majumdar, and P. Yang, Nature **451**, 163 (2008).

[27] P. N. Martin, Z. Aksamija, E. Pop, and U. Ravaioli, Nano Lett. **10**, 1120 (2010).

[28] M. Shelley and A. A. Mostofi, Europhys. Lett. **94**, 67001 (2011).

[29] M. Hu, K. P. Giapis, J. V. Goicochea, X. Zhang, and D. Poulikakos, Nano Lett. **11**, 618 (2011).

[30] X. Chen, Y. Wang, and Y. Ma, J. Phys. Chem. C **114**, 9096 (2010).

[31] C. Patel, W. F. Sherman, and G. R. Wilkinson, J. Phys. C **17**, 6063 (1984).

[32] F. Herman, J. Phys. Chem. Solids **8**, 405 (1959).

[33] G. Leibfried and W. Ludwig, in *Solid State Physics*, edited by F. Seitz and D. Turnbull (Academic Press, New York, 1961), Vol. 12, pp. 275–444.

[34] G. D. Sulka, A. Brzozka, and L. Liu, Electrochim. Acta **56**, 4972 (2011).

[35] X. T. Zhou, T. K. Sham, Y. Y. Shan, X. F. Duan, S. T. Lee, and R. A. Rosenberg, J. Appl. Phys. **97**, 104315 (2005).

[36] P. Caroff, K. A. Dick, J. Johansson, M. E. Messing, K. Deppert, and L. Samuelson, Nat. Nanotechnol. **4**, 50 (2009).

[37] L.-T. Fu, Z.-G. Chen, J. Zou, H.-T. Cong, and G.-Q. Lu, J. Appl. Phys. **107**, 124321 (2010).

[38] Z. Zhong, G. Katsaros, M. Stoffel, G. Constantini, G. Kern, O. G. Schmidt, N.Y. Jin-Philipp, and G. Bauer, Appl. Phys. Lett. **87**, 263102 (2005).

[39] S. Cahangirov and S. Ciraci, Phys. Rev. B **80**, 075305 (2009).

[40] A. N. Cleland, D. R. Schmidt, and C. S. Yung, Phys. Rev. B **64**, 172301 (2001).

[41] X. Zianni, Appl. Phys. Lett. **97**, 233106 (2010).

[42] X. Zianni, Nanoscale Res. Lett. **6**, 286 (2011).

[43] X.-F. Peng and K.-Q. Chen, Physica E **42**, 1968 (2010).

[44] A. Svizhenko, A. Balandin, S. Bandyopadhyay, and M. A. Stroscio, Phys. Rev. B **57**, 4687 (1998).

[45] E. P. Pokatilov, D. L. Nika, A. S. Askerov, and A. A. Balandin, J. Appl. Phys. **102**, 054304 (2007).

[46] D. L. Nika, E. P. Pokatilov, and A. A. Balandin, Appl. Phys. Lett. **93**, 173111 (2008).

[47] J.-S. Wang, J. Wang, and J. T. Lu, Eur. Phys. J. B **62**, 381 (2008).

[48] D. L. Nika, N.D. Zincenco, and E. P. Pokatilov, J. Nanoelect. Optoelect. **4**, 170 (2009).

[49] S. G. Volz and G. Chen, Appl. Phys. Lett. **75**, 2056 (1999).

[50] B. Qiu and X. Ruan, Phys. Rev. B **80**, 165203 (2009).

[51] A. J. C. Ladd, B. Moran, and W. G. Hoover, Phys. Rev. B **34**, 5058 (1986).

[52] A. Ward and D. A. Broido, Phys. Rev. B **81**, 085205 (2010).

[53] D. L. Nika, N. D. Zincenco, and E. P. Pokatilov, J. Nanoelect. Optoelect. **4**, 180 (2009).

[54] P. Giannozzi, S. de Gironcoli, P. Pavone, and S. Baroni, Phys. Rev. B **43**, 7231 (1991).

[55] J. M. Ziman, *Electrons and Phonons* (Clarendon Press, Oxford, 2001), p. 463.

[56] C. J. Glassbrenner and G. A. Slack, Phys. Rev. **134**, A1058 (1964).

[57] N. D. Zincenco, D. L. Nika, E. P. Pokatilov, and A. A. Balandin, J. Phys. Conf. Ser. **92**, 012086 (2007).